Article

Model and Implementation of a Novel Heat-Powered Battery-Less IIoT Architecture for Predictive Industrial Maintenance

Raúl Aragonés [1,2], Joan Oliver [1], Roger Malet [1,2], Maria Oliver-Parera [3] and Carles Ferrer [1,*]

1 Department of Microelectronic and Electronic Systems, Universitat Autònoma de Barcelona, 08193 Bellaterra, Barcelona, Spain; raul.aragones@uab.cat (R.A.); joan.oliver@uab.cat (J.O.); roger.malet@uab.cat (R.M.)
2 Department of Business/Engineering, Alternative Energy Innovations, S.L.—AEInnova, 08224 Terrassa, Barcelona, Spain
3 GIPSA-Lab, CNRS, Grenoble-INP, Grenoble Alpes University, 38402 Saint Martin d'Heres, France; maria.oliver-parera@gipsa-lab.grenoble-inp.fr
* Correspondence: carles.ferrer@uab.cat

Abstract: The research and management of Industry 4.0 increasingly relies on accurate real-time quality data to apply efficient algorithms for predictive maintenance. Currently, Low-Power Wide-Area Networks (LPWANs) offer potential advantages in monitoring tasks for predictive maintenance. However, their applicability requires improvements in aspects such as energy consumption, transmission range, data rate and constant quality of service. Commonly used battery-operated IIoT devices have several limitations in their adoption in large facilities or heat-intensive industries (iron and steel, cement, etc.). In these cases, the self-heating nodes together with the appropriate low-power processing platform and industrial sensors are aligned with the requirements and real-time criteria required for industrial monitoring. From an environmental point of view, the carbon footprint associated with human activity leads to a steady rise in global average temperature. Most of the gases emitted into the atmosphere are due to these heat-intensive industries. In fact, much of the energy consumed by industries is dissipated in the form of waste heat. With this scenario, it makes sense to build heat transformation collection systems as guarantors of battery-free self-powered IIoT devices. Thermal energy harvesters work on the physical basis of the Seebeck effect. In this way, this paper gathers the methodology that standardizes the modelling and simulation of waste heat recovery systems for IoT nodes, gathering energy from any hot surface, such as a pipe or chimney. The statistical analysis is carried out with the data obtained from two different IoT architectures showing a good correlation between model simulation and prototype behaviour. Additionally, the selected model will be coupled to a low-power processing platform with LoRaWAN connectivity to demonstrate its effectiveness and self-powering ability in a real industrial environment.

Keywords: energy harvesting; thermoelectricity; LCA; carbon footprint; LoRaWAN; edge computing; NETZERO; energy intensive industry

1. Introduction

Climate change has clearly accelerated in the last decade. The global average temperature is rising faster than expected. Since the second half of the twentieth century, there has been a steady increase in temperatures due to residual heat, thereby increasing the concentration of greenhouse gases in the atmosphere [1]. The current weather news constantly informs us that we are breaking temperature records. Although the gases that cause the greenhouse effect are diverse, carbon dioxide is the main culprit. It occurs in any activity that involves the combustion of fossil fuels for which industry is largely responsible. Large industries in Europe account for 21% of the energy lost, most of it sent into

the atmosphere in the form of waste heat. It accounts for more than a quarter of primary energy consumption [2].

1.1. Waste Heat Recovery Systems (WHRS)

Many green technologies are currently being investigated to collect energy from different physical domains and transform it into electrical energy [3,4], thus helping to reduce the carbon footprint. One technology being investigated is energy recovery from waste heat. Residual heat is generated in the product transformations in industrial processes. This heat is sent as waste to the environment, causing energy losses. Waste heat recovery systems (WHRSs) [5,6] capture this energy, converting it into useful (electrical) energy and consequently improving the energy efficiency of the industrial processes.

The transduction mechanism is based on the well-known Seebeck effect produced in the thermoelectric generator devices (TEG), popularly called Peltier cells. In line with Carnot's waste heat potential cycle, TEG cells are usually designed to operate in sectors with temperature differential, as large as possible, to increase transduction efficiency. Thermoelectric generators are used in applications that collect heat to produce energy [5–7]. The benefit is two-fold: while generating electricity, the emission of heat into the atmosphere is reduced.

In addition, restrictions that are being imposed by governments on waste energy are increasing the investment and research of these technologies [8], which can result in device efficiency improvement. The key point in the improvement of these devices is in the performance of the semiconductor materials used in the TEG cells [9,10]. The use of TEGs as elements of a WHRS is increasingly being used by the industry [11–14]. Another example is the WHRS mounted in Bodegas Torras [15], which checks the condition of a pellet stove in an environment that works at 150–300 °C and is used to collect residual heat. A key aspect of energy conversion efficiency lies in being able to keep the hot side of the TEG at a high temperature, while the cold side stays cold and does not heat up. That is why the use of a WHRS is becoming evident in the automotive [16] and aeronautical [17] industries.

1.2. WHRSs in IoT and Harsh Environments

The capacity of thermoelectric devices to harvest thermal energy and convert it into electrical energy is still small for power systems that demand a large amount of energy. In accordance with [18], thermal energy is abundant and can be transformed into electrical energy using the TEG modules. It is also clean, constant, and it is an efficient energy transduction method.

WHRSs have advantages that make them unique in IoT applications where power requirements are small. They can harvest enough energy to power wireless IoT applications. It is envisaged as one of the major areas where TEG devices can power enough energy to power small devices [3,18,19], like industrial wireless sensors and wearables [20]. Today, almost 100% of these devices are powered by lithium batteries, which commonly store from 3000 mAh to 8000 mAh, and are expensive consumption devices and large pollutants. A recent Life Cycle Assessment (LCA), developed internally by the authors at AEInnova, estimated that the environmental impact of an 8000 mAh battery is equivalent to 400 kg of CO_2.

In addition, these industrial systems powered by batteries have drawbacks that reduce battery lifetime and limit their adoption in heat-intensive industries. In general:

- They use low-range wireless protocols, which implies expensive costs in wireless infrastructures (i.e., WirelessHart or ISA100 protocols).
- They have a low data rate (sending data from 1 time per hour to 1 time per day).
- They do not process data in the node (edge computing), which implies the need to move computerized data to the cloud (with more costs and carbon footprint).
- Heat affects their durability, reducing their lifetime by more than 20% when the temperature is above 80 °C [21].

Autonomous non-battery-powered systems can also work in explosive industries (oil and gas, chemical, paper, wheat, etc.). In these facilities, devices must pass the atmosphere explosive proof, requiring a very complex certification (ATEX or IECEX). Devices wearing explosive lithium batteries cannot be used in these installations. A WHRS can harvest enough energy from any hot surface of the installation, thus allowing the self-powering of sensing nodes in any difficult access place of the facility, without the need for electrical power distribution. In addition, WHRSs can power these nodes in ATEX areas where batteries or power grids can be potentially dangerous.

1.3. WHRS Modelling

This paper presents and compares the mathematical model of a WHRS architecture for IoT nodes. The complete thermoelectric system model considers the contribution of the TEG cell in conjunction with all the elements that constitute a WHRS.

A model is used for the thermoelectric device that considers its dynamic behaviour when transforming heat energy into electrical energy [5,7,15]. However, the manufacturers of TEG do not provide the physical parameters of them. That is the Seebeck coefficient, thermal conductivity, and thermal resistivity. They must be calculated using the figures in the technical datasheet of the TEG devices. For this, the calculation of *effective parameters* of the TEG is used [22–25]. In the WHRS, the TEG device is enclosed between a collector and a heatsink. The contribution of all the components in the thermal path heat propagation is passive and it is modelled as thermal resistors or capacitors. The resistive thermal paths of the contacts between components [26] and the behaviour of the heatsink fins are also considered [27] due to the large impact they have on heat propagation and thus on system efficiency.

Based on these considerations, this paper summarizes the methodology followed in the modelling and behavioural simulation of Waste Heat Recovery Systems for IoT nodes (IoT-WHRS) and presents a first pilot in a real industrial environment.

The final application, selected to test the model, is one of the most demanding in Industry 4.0: vibration monitoring. Performing these monitors on rotary machines (motors, pumps, fans, compressors, gearboxes, etc.) for predictive maintenance has several benefits in the form of overall energy savings, as well as reducing breakdowns, downtime, etc. (Figure 1). A final pilot was installed at the PREZERO leachate plant in Santa Maria de Palautordera (Barcelona, Spain).
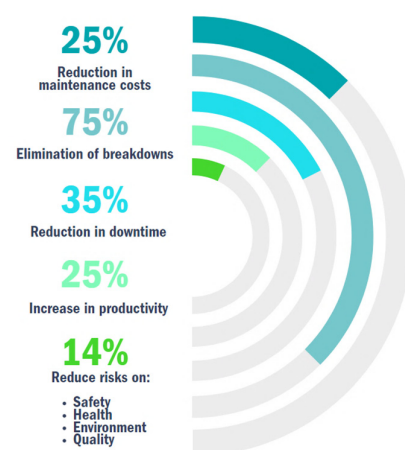
Figure 1. Predictive maintenance savings in rotative machines.

The paper is structured as follows: Section 2 introduces the IoT-WHRS architecture for IoT applications. The IoT-WHRS modelling methodology is presented in Section 3. Section 4 calculates the effective parameters of the TEG. Section 5 presents the finite difference model of the IoT-WHRS. The results of the simulation are presented in Section 6. Section 7 introduces the low-power IoT device. Sections 8 and 9 present the results of the

experimental and statistical analyses. The conclusions summarize this work and discuss the future possibilities of the IoT-WHRS.

2. WHRS Architectures for IoT

Low power consumption is one of the most important requirements in wireless sensor network applications. Low power is usually required in the processing stage of the IoT nodes, while high-demand bursts of power [18,19] are required for data transmission. This energy demand profile makes thermoelectric cells mounted on IoT-WHRS suitable for powering IoT nodes. Energy can be constantly harvested from heat losses in the facility and stored. Power can then be distributed during the IoT node cycle with the data acquisition, processing, and transmission stages. Currently, the power efforts of the IoT nodes are being combined with algorithms that analyze optimal power consumption in the IoT network and distribute the collected energy to the prioritized IoT nodes [28].

Figure 2 shows the data and power channels of a wireless IoT node powered by power harvesting. The upper channel corresponds to the data acquisition channel in a smart sensor. The data, once processed, are sent to the communication channel, either to other nodes that make up the sensor network or to the processor in charge of receiving the data.
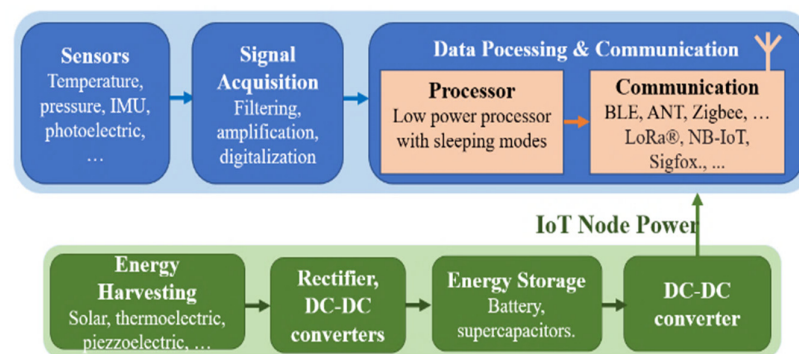

Figure 2. Energy-harvesting architecture in IoT nodes.

The lower channel of the figure details the components used in the energy-harvesting stage to obtain the supply voltage for the IoT nodes. The energy received by the transducer is rectified and regulated to be stored in a rechargeable battery, capacitors, etc. Thus, the IoT node is only powered when energy is required [29]. The harvesting circuit is responsible for collecting energy.

The architecture of an IoT-WHRS is complex. It must combine mechanical and electronic parts in environments that operate at high temperatures. It must achieve the lowest thermal resistance between the TEG, the collector, and the heat-dissipating elements.

The harvested power from a thermoelectric device depends on the ability to maintain a low temperature on the cold side of the module, while the high temperature is harvested on its hot side. The efficiency of the IoT-WHRS depends on the ability of the system to harvest as much heat as possible while maintaining a large temperature difference between both sides.

According to the laws of thermodynamics, the natural tendency of the TEG is to balance the temperature of both plates. This is carried out by dissipating heat caused by internal thermal resistance, the heat collector and the heatsink. This plays a crucial role in the efficiency of the overall system. Everything is clamped to minimize gaps in the contact module.

The holding mechanism creates an air gap within the IoT-WHRS which, due to the inherent thermal cooling capacity of the air, influences the efficiency of the system. This behaviour is clear in the IoT-WHRS presented in this paper. It has a large collector area to keep the TEG face warm at maximum temperature, and a large heat-dissipating surface to

cool it to the maximum. Due to the clamping mechanism, it has an air gap channel with a thermal capacitance that influences the efficiency.

Figure 3 corresponds to the IoT-WHRS. It consists of (1) the GM200-161-12-20 Peltier cell (European Thermodynamics Ltd., Leicestershire, UK), (2) the base formed by a copper plate, which constitutes the thermal collector, and (3) an Al6063-T5 radiator with aluminum fins. Natural convection is used to dissipate heat from (4), the cold face of the TEG, the collector and the heatsink.
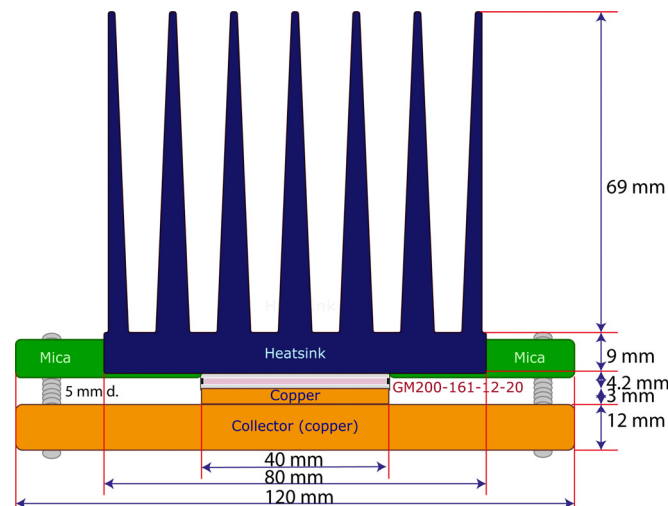

Figure 3. IoT-WHRS and dimensions. The TEG cell is placed between the heat source under the collector and the heatsink.

These blocks are fixed by means of a support that has a surface equal to that of the collector. This creates an empty space between the two surfaces filled with air. Finally, (5) a 3 mm high piece of copper, is placed between the collector and the TEG device. However, it creates a resistive thermal path in the vicinity of the TEG that separates the collector from the heatsink.

3. IoT-WHRS Model Parametrization

The thermal and electrical properties of materials must be considered when modelling the IoT-WHRS. The TEG cell is interspersed between the mechanical parts responsible for collecting heat and dissipating it.

The power generation of the system is provided by the capacity of the TEG transducer. The capture, propagation, and dissipation of heat depend on the architecture of the system and the materials used. The contribution of all the components to heat flow is modelled by thermal resistances and thermal capacitances. The thermal resistances and thermal capacity of the components depend on their physical dimensions and thermal properties. Table 1 summarizes the properties of the materials used in the IoT-WHRS.

The density, thermal conductivity, and specific heat properties of the material determine the thermal resistance and capacity of the components. Micro-hardness and surface roughness determine the contact performance between components.

Circuits such as those used in the analysis of the electrical circuits model the thermal behaviour of the system [30,31]. An IoT-WHRS must consider the TEG devices, heatsink and the contact between materials. The TEG is modelled on the properties of the pellets, the ceramics, and the welding materials [25]. Due to the difficulty in obtaining the manufacturer's TEG specifications, the effective parameter model is used [22]. The model of effective parameters is discussed in Section 4.

Table 1. IoT-WHRS material properties.

	Units	Air [*]	Copper	Al6063-T5	Alumina 96%, Al_2O_3	Graphite	Mica
Density	ρ, (Kg/m^3)	1.1839	8900	2700	3750	1800	1000
Thermal conductivity	K, (W/(mK))	0.0261	385	209	20	5	0.3
Specific heat	Cp, (J/(kgK))	1004.3	385	896	900	895	900
Micro-hardness [**]	μH, (MPa)		1500	670	14,700	100	50
Surface roughness [**]	sR, (μm)		2.6	1.8	1.0	2.0	5.0

[*] Air is treated as an ideal gas at atmospheric pressure due to its low density. The parameters are taken at T = 25 °C. [**] Micro-hardness and surface roughness are used in the calculation of contact resistance. The roughness of the surface depends on the method of cutting and polishing.

The heat dissipation in the heatsink is different on the base than on the fins. The heat propagates to the base of the heatsink, which is in contact with the TEG. The heatsink fins dissipate heat in the environment, being primarily responsible for cooling the system. The efficiency depends on the material and geometry of the fins. A good discussion of fin modelling as heat exchangers can be found in [27].

Any contact between the materials also creates thermal resistance to heat transfer. As specified in Yovanovich [26], contact strength is difficult to calculate because it depends on the specific heat of materials and the micro-hardness of the materials, which affects the calculation of the thermal resistance of contact and roughness of the material. It depends on the shape and type of cutting of the material. It is measured in μm. The micro air gaps that the cut creates impact the resistance to thermal contact.

3.1. IoT-WHRS RC Model

Figure 4 details the thermal resistances and thermal capacitances involved in the model of the IoT-WHRS. The components of the system act as heat-resistive elements in heat transfer.

Figure 4. RC model of the IoT-WHRS. As the IoT-WHRS model is symmetrical, the figure only shows its left side.

The heat retention capacity is determined by the specific heat capacity of the materials. The thermal resistance and thermal capacity of the air gap are also considered. The IoT-WHRS creates two clear paths of heat propagation: the thermal path that includes the elements enclosed by the TEG and the thermal path formed in the air channel. The elements that contribute to heat distribution and propagation are:

- The copper collector and the piece of copper between the collector and the TEG.

- The TEG device. The thermoelectric effect, the ceramic plates and the weld joining to the ceramic plates are considered. Q_{hot} and Qcold explain the rejection and absorption of heat in the TEG.
- The heatsink and heatsink fins.
- The contacts between these components are thermal heat resistances to the heat propagation.
- The volume of the air gap.

From Figure 4, it is easy to build the complete RC model of the IoT-WHRS. Figure 5 shows all the thermal resistances and capacitances that contribute to thermal propagation. The thermal circuit must also include the dynamic behaviour of the TEG for model correction. As introduced, heat propagation in the IoT-WHRS is performed in two channels.
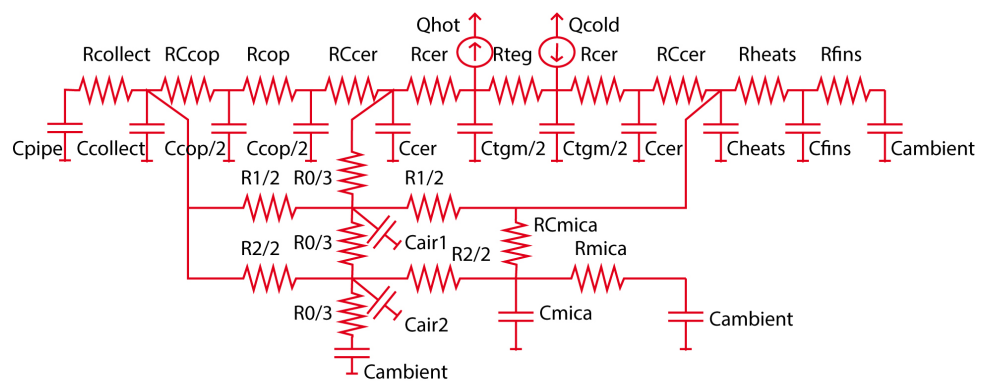
Figure 5. Detailed thermal IoT-WHRS RC circuit. Thermal resistors and heat capacitors model the flow of heat through the system.

3.2. Heat Propagation Contribution of the TEG Channel

All the elements have responsibility for heat transfer. According to [22,24], the TEG model considers the thermal resistance and the thermal heat capacitance of the pellets, named R_{teg} and C_{teg}. Both values depend on temperature and must be recalculated at each step of the simulation and ceramic (alumina material) that encloses the pellets, named $R_{ceramics}$ and $C_{ceramics}$.

These parameters are calculated based on thermal conductance, heat capacity and alumina geometry. The model does not include the thermal resistance of the aluminum that interconnects the pellets because it considers it the model of effective parameters of the TEG (Section 4).

The collector is made of copper material. It is modelled with a thermal resistance $R_{collector}$ and thermal heat capacity $C_{collector}$.

Similarly, the collector/TEG separator, a copper plate, with a R_{copper} thermal resistance and a C_{copper} thermal heat capacity are modelled.

The heatsink model is more complex. The base and fins are considered separately. The base is modelled as in the case of the collector plate, with $R_{heatsink}$ and $C_{heatsink}$. The behaviour of the fins [28] is modelled with R_{fins} and C_{fins}.

The heat is absorbed in the hot surface by the collector and returned to the environment by the heatsink.

The hot surface and environment are modelled as high thermal heat capacitors, C_{pipe} and $C_{ambient}$, infinite in the model.

In the figure, all RC_{xx} resistors account for the thermal contact resistances [26].

3.3. Contribution of the Air Gap Channel to the Heat Propagation

The air gap channel is an internal air gap created by the clamping mechanism that fixes the TEG between the collector and the heatsink. The volume of air created influences the overall performance of the system thus contributing to the propagation of heat in the volume around the TEG. The air is closed between the collector, the aluminum base of the heatsink, and mica (insulator with high thermal resistivity).

Due to the different materials that enclose the air, the air gap channel is modelled with the following thermal resistances and thermal capacities: the transversal heat propagation channel between the environment and TEG is modelled by the thermal resistance R_0; the thermal resistance R_1 corresponds to the thermal channel between the heatsink and the collector; thermal resistance R_2 accounts for the mica collector heat transfer channel; and the C_{air1} and C_{air2} capacities model the heat channel capacity.

4. TEG Efficient Parameters Model

The performance of IoT-WHRS depends on the efficiency of the TEG device in the conversion of thermal energy into electric energy. Its energy generation is the result of the conjunction of the Seebeck, Peltier, Thomson and Joule physical phenomena that occur in the thermoelectric semiconductor devices (pellets), according to Table 2 [22,23]. Performance, in terms of energy production, is maximized by increasing the Seebeck effect, while reducing heat transfer. The main responsible for heat transfer in the TEG is the internal resistance R0. The ηmax efficiency coefficient of the TEG explains it. The Z-merit figure is taken as a parameter to compare performance.

Table 2. TEG thermoelectric model. E, $\dot{Q}$, T. I, α, σ, κ and R_0 means electromotive force (V), heat flow (W), temperature (K), current (A), Seebeck coefficient (V/K), electrical conductivity (S/m), thermal conductivity (W/(mK)), and electrical resistance (Ω), respectively. Figure of Z-merit units are 1/K.

Seebeck effect:	$\frac{\partial E_T}{\partial T} = \alpha_a - \alpha_a$
Peltier effect:	$\dot{Q}_{Peltier} = \pm IT(\alpha_a - \alpha_b)$
Thomson effect:	$\dot{Q}_{Thomson} = -\sigma I \Delta T$
Joule effect:	$\dot{Q}_{Joule} = R_0 I$
Efficiency coefficient:	$\eta_{max} = \frac{T_H - T_C}{T_H} \frac{\sqrt{1-Z\overline{T}}-1}{\sqrt{1+Z\overline{T}} - \frac{T_C}{T_H}}$
Figure of merit:	$ZT = \frac{\sigma \alpha^2 T}{\kappa}$

To simulate the behaviour of the TEG within the IoT-WHRS, the thermoelectric parameters α, σ and κ must be known. Unfortunately, these parameters are usually not provided by the manufacturer. To do this, the effective parameters α^*, κ^*, ρ^* and Z^* of the cell are calculated from the TEG datasheet, introducing negligible errors in the model [15,22]. According to Table 3, effective parameters are calculated using the maximum power characteristics Wmax, electromotive force Vmax, current Imax, and efficiency ηmax. n is the number of thermocouples of the TEG.

Table 3. Effective parameter equations. ηc = 1 − T_H/T_C is the Carnot efficiency.

$$\alpha^* = \frac{4W_{max}}{nI_{max}(T_h - T_c)}$$
$$r^* = \frac{4\left(\frac{A}{L}\right)W_{max}}{n(I_{max})^2}$$
$$k^* = \frac{(\alpha^*)^2}{\rho^* Z^*}$$
$$Z^* = \frac{2}{T_c\left(1+\left(\frac{T_c}{T_h}\right)^{-1}\right)}\left[\left(\frac{1+\left(\frac{\eta_{max}}{\eta_c}\right)\left(\frac{T_c}{T_h}\right)}{1-\left(\frac{\eta_{max}}{\eta_c}\right)}\right)^2 - 1\right]$$

Kryotherm GM200-161-12-20 is used in this study. Table 4 summarizes the specifications and effective parameters calculated using the equations given in Table 3.

Table 4. GM200-161-12-20 specifications and calculated effective parameters.

Thermoelectric Parameters		
Number of pellets, n	199	
Maximum power (Th = 200 °C), W_{max}	5.3	W
Max. voltage (no load), V_{max}	11.2	V
Max. current, I_{max}	1.88	A
Max. efficiency, η_{max}	5.6	%
Matched load resistance (200 °C), R_L	5.9	Ω
Effective Parameters		
Effective Seebeck coefficient, α^*	3.33×10^{-4}	V/K
Effective thermal conductivity, κ^*	1.94	W/(m·K)
Effective resistivity, ρ^*	3.8×10^{-5}	Ω·m
Figure of merit Z^*	1.6×10^{-3}	1/K
Figure of merit ZT^*	0.48	

5. IoT-WHRS Finite Difference Model

The IoT-WHRS system simulation considers the energy variations that occur in the system due to the flow of heat from the temperature of the pipe (hot) to the ambient temperature (cold). The system is restricted so that the electrical power obtained from the collection must be equal to the energy provided by the difference in heat flow in the system, $Q_H - Q_C$.

The heat flux equations describing the temperature distribution can thus be written as a system of partial differential equations that have a continuous character [30,32]. In addition, the heat generation at each simulation step depends on the temperature, thus creating a non-linear system. The mathematical solution of this non-linear system of differential equations is not analytically affordable. Taking the equation as a system of finite difference and with an initial T_{pipe} (the hot surface) and final environment $T_{ambient}$ (the cold surface), the evolution of the internal temperatures of the system is calculated by an iterative process. The power delivered by the TEG depends on the temperature on its cold side and the difference between the sides.

A numerical approach to the solution of these equations is to discretize and write the corresponding set of differences in Equation (1) [22,24].

$$\left(1 + \frac{\delta t}{C_a} \sum_{b=1}^{n} \frac{1}{R_{a,b}}\right) T'_a - \frac{\delta t}{C_a} \sum_{b=1}^{n} \frac{1}{R_{a,b}} T'_b = T_a + \dot{Q}_a \frac{\delta t}{C_a} \tag{1}$$

In Equation (1), subscripts a and b represent neighbouring nodes linked by the thermal resistance $R_{a,b}$.

In the equation (as in the model of Figure 5), T represents the current nodal temperature, T' the nodal temperature to be calculated in the current δt iteration, $R_{a,b}$ the resistance between both nodes, Ca is the thermal capacity associated with the node, and $\dot{Q}_a$ the heat generation in the node.

The terms of the matrix (represented in (1) by the term in the parentheses) are obtained from these parameters of thermal resistance and thermal capacity according to the model links. For example, the IoT-WHRS model contains 14 nodes, thus creating a 14 × 14 term matrix (2):

$$\begin{pmatrix} m00 & m01 & 0 & & 0 & 0 & 0 \\ m10 & m11 & m12 & \cdots & 0 & 0 & 0 \\ 0 & m21 & m22 & & 0 & 0 & 0 \\ & \vdots & & \ddots & & \vdots & \\ 0 & 0 & 0 & & mbb & mbc & 0 \\ 0 & 0 & 0 & \cdots & mcb & mcc & mcd \\ 0 & 0 & 0 & & mdb & mdc & mdd \end{pmatrix} \tag{2}$$

Each term of the matrix is obtained from the model connections. For example, the first six and last six non-zero terms of this matrix are given by the following equations, all obtained from the links of Figure 5:

$$m00 = 1 + (dt/C_{pipe}) (1/R_{col})$$

$$m01 = -(dt/C_{pipe}) (1/R_{col})$$

$$m10 = -(dt/C_{col}) (1/R_{col})$$

$$m11 = 1 + (dt/C_{col}) (1/R_{col} + 1/R_{ccop} + 1/R_{1/2} + 1/R_{2/2})$$

$$m12 = -(dt/C_{col}) (1/R_{ccop})$$

$$m19 = -(dt/C_{col}) (1/R_{1/2})$$

$$\dots$$

$$mcc = 1 + (dt/C_{fins}) (1/R_{heats} + 1/R_{fins})$$

$$mcd = -(dt/C_{fins}) (1/R_{fins})$$

$$mda = -(dt/C_{amb}) (1/R_{0/3})$$

$$mdb = -(dt/C_{amb}) (1/R_{mica})$$

$$mdc = -(dt/C_{amb}) (1/R_{fins})$$

$$mdd = 1 + (dt/C_{amb}) (1/R_{0/3} + 1/R_{mica} + 1/R_{fins})$$

In the equation, several terms depend on temperature and must be calculated at each simulation step. At each step of temperature, the system of finite difference equations is iterated, with the added difficulty of having to invert the state matrix to find current temperatures. In addition, at each step, all temperature-dependent parameters must be recalculated. It affects the thermal resistance of the fins, the thermal resistances and capacities of the air gap, the thermal resistance of contacts and the heat flow in the TEG.

6. Simulation Results

Table 5 presents the setup parameters for the IoT-WHRS simulation, that corresponds to the setup of the devices under test. R_{load} is the external electrical resistance coupled to the system to match the internal electrical resistance of the thermoelectric device to obtain the maximum power. The torque, force, and screw diameter account for the fixing mechanical parameters that clamp the thermoelectric device to the collector and heatsink.

Table 5. Simulation conditions and model parameters.

Simulation Setup Parameters	
Rload	=10.0 Ω
Torque	=0.7 N/m
Force	=875,000 Pa
Screw diameter	=5 mm ⌀

The parameters of the IoT-WHRS model are obtained from the physical characteristics of the components used (Figure 4) and the properties of the materials (Table 1). The contact resistances and dissipation capacity of the fins are calculated according to [26,27].

Figure 6 represents the results of an IoT-WHRS simulation. The top row presents the evolution of temperature, and the bottom row presents the power delivered by the systems. The simulation performs a T_{hot} range from 25 °C to 225 °C, while T_{cold} is maintained at 25 °C. The bottom row shows the power delivered by the system. As should be the case,

the heat power harvested (WT) corresponds to the electrical power generated (WE). The power supplied by the two IoT-WHRS architectures is similar.
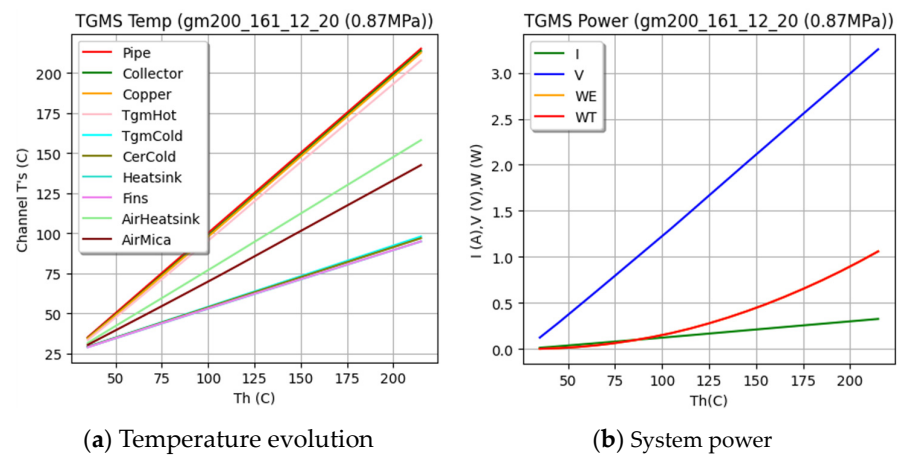

(**a**) Temperature evolution

(**b**) System power

Figure 6. IoT-WHRS simulation results. Temperature evolution and power of the system.

7. Low-Power Autonomous Hardware Architecture

The specifications for the vibration monitoring are selected based on the benefits of predictive maintenance for Industry 4.0 (Figure 1). It is required to acquire vibrations in rotative machines with at least one piece of data per day to have an accurate diagnosis of the machine under test. The diagnosis is performed following the norm DIN ISO 10816-3 [33]. The full solution architecture is proposed in Figure 7.
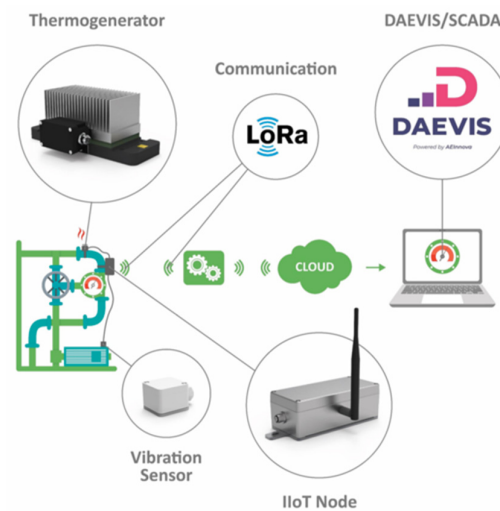
Figure 7. Full hardware and software platform.

The system is composed of a thermoelectric generator (selected IoT-WHRS) attached to a hot surface, an IoT communication device and a three-axis vibration sensor installed on the rotative machine we want to monitor. Finally, a LoRaWAN gateway communicates with a data visualization platform (DAEVIS—Dynamic AEInnova Visualizer) or a SCADA.

To perform the monitoring process, the algorithm that performs all acquisition and communication processes was optimized (Figure 8). Data were converted from the acceleration domain to the velocity domain as requested by ISO 10836-3. The process involves a 1000 Tones FFT calculus. The system builds a waking up and deep sleeping down cycle to meet the highly restrictive power generation coming from the thermoelectric generator. The wireless sensor network includes an MQTT protocol with authentication to avoid cyber-security issues.
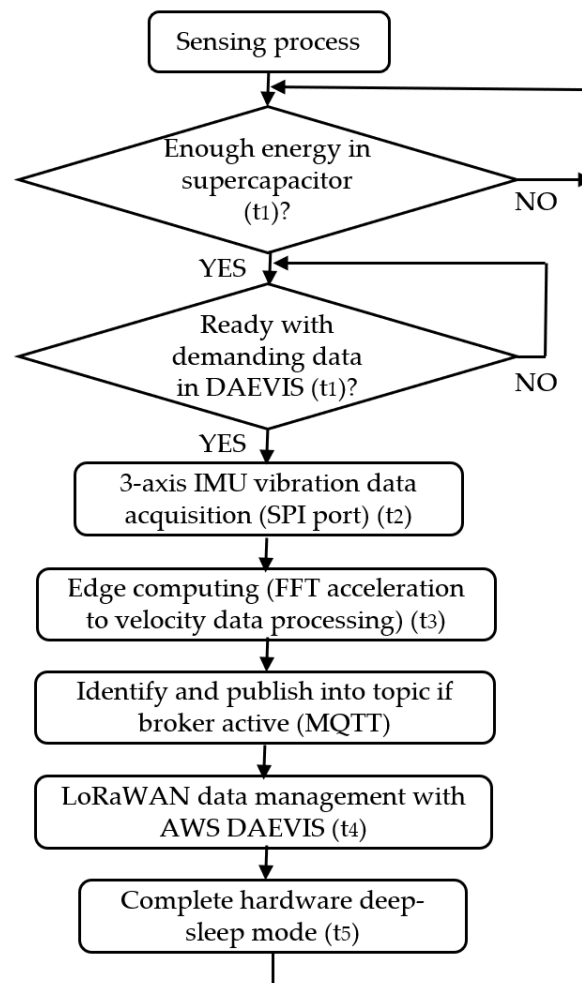
Figure 8. Full acquisition, processing, and communication algorithm.

8. Experimental Results

8.1. TEG Module Experiments

The devices were tested with a temperature range from room temperature to 200 °C. The temperature and power of the system were recorded by placing temperature sensors in the WHRS (Figures 3 and 4). The electrical and mechanical parameters maintained the values specified in Table 5.

The test was performed by heating the collector of IoT-WHRS. The system was heated until the collector temperature stabilized at around 200 °C (Figure 9). Then, it was allowed to cool down to room temperature. Several heating/cooling cycles were performed per experiment.

The time spent in each experimental session depends on the number of completed heating/cooling cycles, with an average time of one hour for heating and one hour for cooling. Temperature is taken per second at the specified system locations. The temperature T_{pipe} in the graphs corresponds to the collector; in the copper separator it is T_{copper}; at the base of the heatsink, $T_{heatsink}$; at the base of the fins, it is $T_{basefins}$; on the tip of the heatsink fins, T_{fins}; room temperature is also measured. The plot above shows the temperature variation measured in heating and cooling. At high temperatures, the dispersion in temperature is due to the lower sensitivity of thermistors at high temperatures. The plot below shows the voltage, current and power measured.
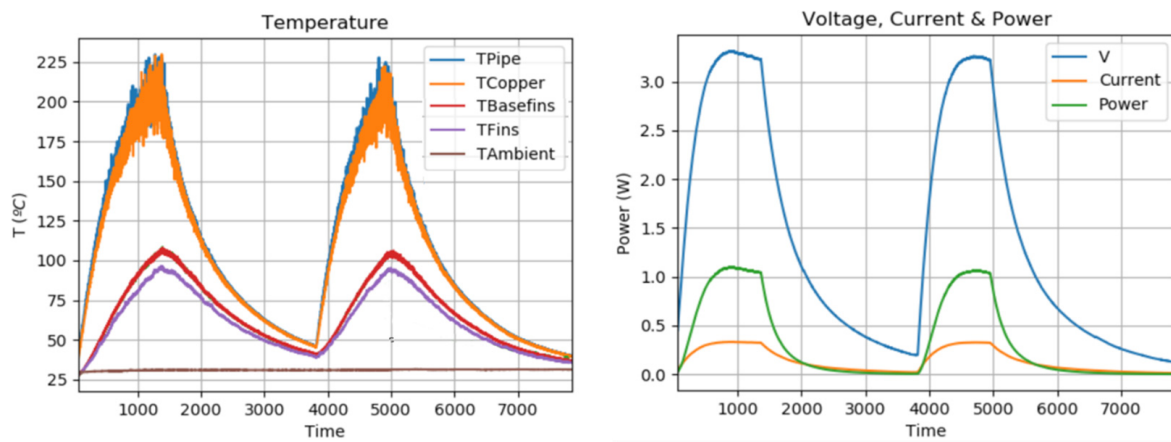
Figure 9. Temperature evolution (**left**) and power generated (**right**) results on IoT-WHRS heating and cooling test (data normalized in W, V, and A).

The results obtained are consistent with the simulation results. The behaviour of the power given by the system during the heating and cooling cycles is the same, which is expected because the power is a function of the hot side temperature and the temperature difference between the TEG plates.

8.2. Experimental Data Analysis

Several experiments were performed using three GM200-161-12-20 thermodynamic cells to analyze the behaviour of the IoT-WHRS (Figure 10). A total of 21 tests with heating and cooling cycles were performed. The points represent the mean values and the crosses represent the variability. The figure shows the good behaviour of the cells in each IoT-WHRS. The power generated is similar for each thermoelectric cell, remaining inside the error bar.
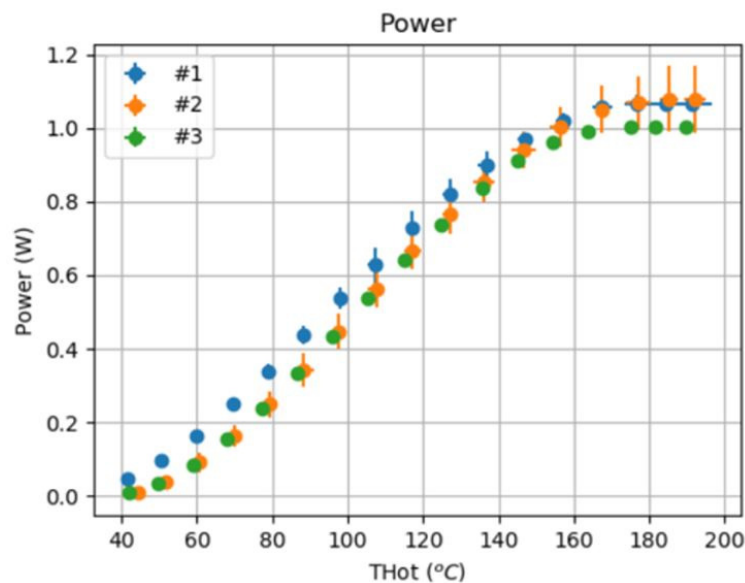
Figure 10. Power graph of the IoT-WHRS.

Figure 11 compares the experimental power obtained with respect to the theoretical one based on the temperatures of the hot face and cold face. The experimental results show a lower performance (ranging from 10% to 28%) than the theoretical one. One factor influencing this error is the application of the effective parameters model that introduces errors of around 10% at average temperatures and depends on the temperature on the cold face.
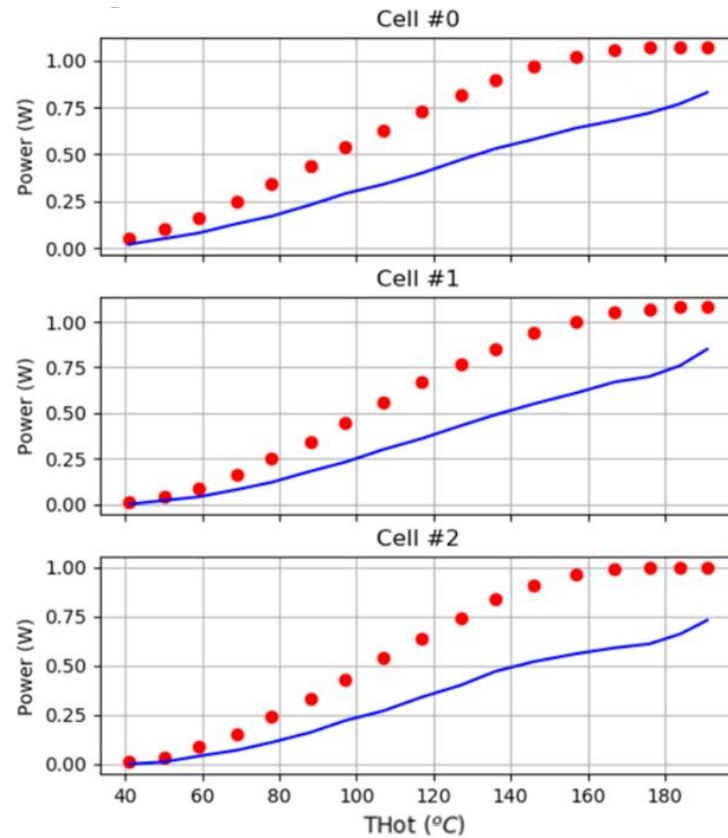
Figure 11. These graphs show theoretical power computation (red dots) with respect to experimental power (blue line) as a function of the hot face and the cold face temperatures.

8.3. IoT Module in the Facility

Following the conceptual diagram of Figure 2, the IoT device is designed once the energy profile created in the previous subsection is obtained. The obtention of up to 1 W of power is enough to carry out a complete acquisition, processing and communicating cycle. The IoT module uses the following commercial components:

- The low-power cortex M4 processor (STM32L4) as the processing device.
- The Microchip LoRaWAN chipset (RN2483).
- IMU ST-Microelectronics (ISM330DLC) for the vibration monitoring.

Figure 12 shows the energy profile of the IoT module using the edge processing algorithm explained in Figure 8. The upper graph represents the current consumption, and the lower graph represents the power consumption of the module. To represent from T_1 to T_4 (Figure 8 over Figures 12 and 13) it was alternatively fitted for a better representation and understanding. Figure 12 shows:

- The total duration of the process is 9.66 s.
- The overall consumption of a cycle containing acquisition, processing and communication is only 74.6 µWh.
- The maximum power peak of 105 mw (a peak of 42 mA in current) occurs when the chipset links with the gateway.

Figure 13 shows the same process including the *deep sleep mode* time (T_5). In this case:

- The acquisition process cycle repeats every 60.422 s.
- The overall consumption (T_1–T_5) is 95.6 uWh.
- The deep sleep mode of the system is only 1.47 mW.

Figure 12. Energy profile of the IoT + vibration sensor from T_1 to T_4. With a total duration of 9.66 s.

Figure 13. Complete energy profile of the IoT including the deep sleep time T_5.

8.4. Hardware Integration in a Real Pilot

Figure 14 shows the PoC deployed in the leachate plant of PREZERO in Santa Maria de Palautordera (Spain) to demonstrate the full application of the system. The system allows us to test the complete edge computing and heat-powered module in a real environment.
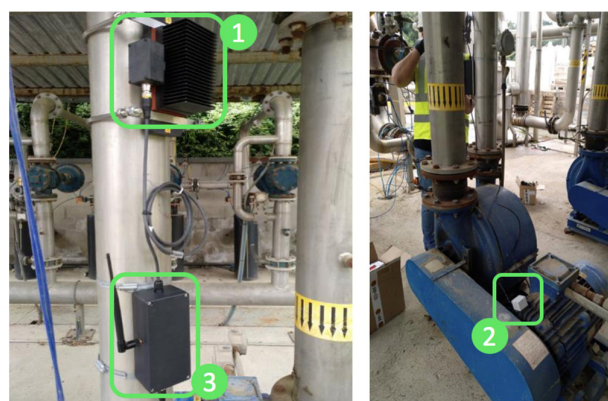

Figure 14. 1. Thermoelectric generator; 2. vibration sensor; 3. the LoRaWAN IoT device.

The system uses the thermoelectric generator (IoT-WHRS) attached to a hot surface (a smokestack (1)), the IoT communication device (3) and a three-axis vibration sensor (2) installed on the rotative machine to monitor it (a 15 KW combustion fan). Finally, a LoRaWAN gateway sends data packets to the IoT core located in DAEVIS, a cloud platform developed under Amazon Web Services.

Figure 15 shows the registration of the rotative machine vibrations for a time span of four months, which goes from the first tests in our laboratory (6 to 9 of June) to the final test installed in the combustion fan of Santa Maria Palautordera (5 to 8 of September). The figure monitors critical vibrations in the combustion fan during all four days, and we applied a zoom on 7th of September.

Figure 15. Results of four-day tests in the combustion fan.

The monitored machine is classified as *Machine Group 4*, with a rigid base on the ground. From the data obtained, the health of the machine can be known according to the ISO Standard [33], which defines the critical speeds as:

- Healthy machine: from 0 mm/s to 1.4 mm/s.
- Short-term operation allowable: from 1.4 mm/s to 4.5 mm/s.
- Vibrations cause machine damage: from 4.5 mm/s to unlimited.

The figure shows that there are several fractions of time on days 2, 3 and 4, which significantly overpass the damaging values of 4.5 mm/s, meaning that this machine requires rapid maintenance to avoid critical damage.

Figure 16 shows different temperature increment intervals (ΔT) tests with different air flow combinations and motors with different motor misalignments. These assays were performed in the lab for a full characterization (Table 6). They considered different combinations of ΔT and air flow and the data cadence sent to the cloud was also compared. A decrease in data rate was observed when ΔT increases. Higher air flow also reduces data rates. In addition, misalignments introduced to the rotor of the same 350 W electric motor corroborate that the motor vibrations decreased (d) or increased (e).
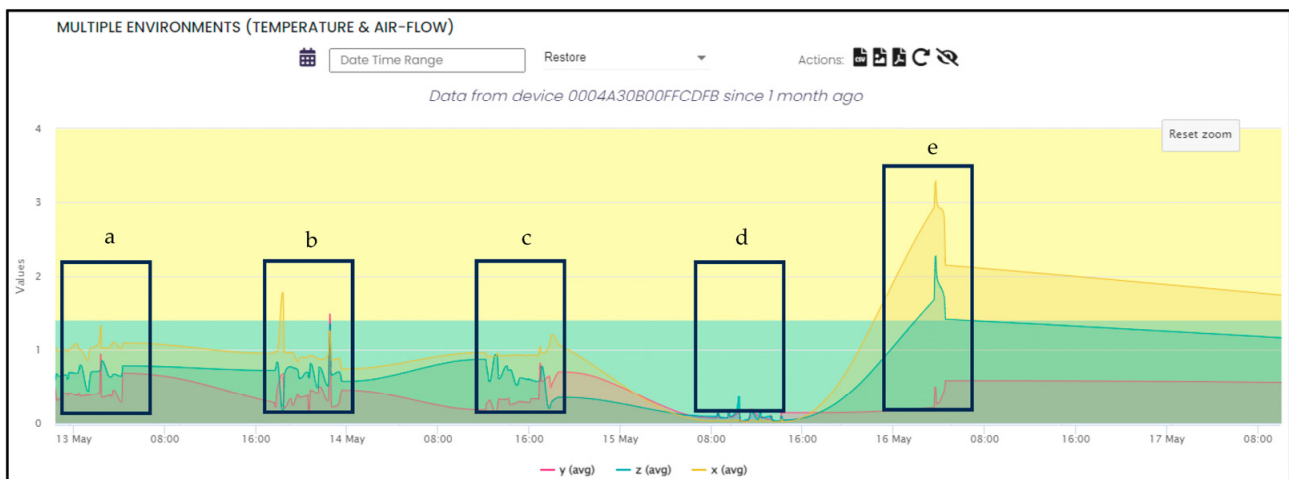

Figure 16. Multi-environment test. The boxes show temperature increases related to wind flows.

Table 6. Multi-environment assay.

Case	ΔT	Air Flow	Data Cadence	Motor Type.
A	125 °C	0 m/s	5	350 W with small misalignment.
B	100 °C	0 m/s	7	350 W with small misalignment.
C	75 °C	5 m/s	10	350 W with small misalignment.
D	50 °C	10 m/s	10	350 W without misalignment.
E	25 °C	0 m/s	30	350 W with big misalignment.

The technology introduced with the WHRS-IoT can be used in all industrial sectors that need to work with medium temperatures and with the need to power devices with small amounts of energy. Table 7 resumes this potential application per industry sector, detailing the application case per section of the process and working temperature process.

Table 7. WHRS-IoT applicability by industrial sector, process and working temperature range.

Industrial Sector	Section of the Process	Temperature Range °C
Iron and steel production Ferrous metals processing	Basic oxygen steelmaking	200
	Re-heating and heat treatment furnaces radiation	240
Cement industry	Steam and gas exhausts	130–220
	Co-generation/combined heat and power	100
Chemical and petrochemical Large volume inorganic chemicals solid industry	Sulphur burning processes	145
Chemical and petrochemical Large volume inorganic chemicals, ammonia, acids and fertilizers	Conventional steam reforming: desulphurization processes	350–400
	Conventional steam reforming: primary and secondary reforming	Primary: 400–600 Secondary: 400–600 Exhaust gas: 1000
Chemical and petrochemical Surface treatment using organic solvents	Drying and curing	300–700
	Manufacturing of abrasives	35–110 in the drier 700 for the exhaust air
	Coil coating	150–220
Food and tobacco Food, drink and milk industry	Heat recovery from cooling systems	50–60
	Winery exhausts	200–240
	Alcohol distillation exhausts	130–220
Wood Wood-based panel production	Drying of wood particles	60–220
	Pressing	100–300
Paper and printing Paper and board production	Paper making and related processes	150–300 (exhausts) >350 (Coated wood-free printing tissue processes
Textile and leather Textiles industry	Tanning and hide drying	60–90
	Drying	130
Non-specific industry Waste treatment	Drying and degassing	100–300
	Drying	100
	Dying of wood particles	200–370 for single/triple pass dryers 500 at rotary dryers

9. Conclusions

The paper presented an IoT-WHRS model and testing was used to power a specific IoT device to monitor vibrations in complex facilities. The WHRS harvests energy from waste heat sources at medium temperatures. The module was modelled and tested with coherent results. The main benefits offered by this thermal harvester device are clear: IoT devices can be powered by harvested energy without the need to use other energy. These IoT nodes can be installed anywhere without the need to use a power grid or batteries, and devices may operate in critical facilities where an electrical power supply is not recommended. The benefits offered by these WHRS modules are aligned with:

- The new EU regulations (12 July 2023) of battery usage in any device [34].
- The reduction in maintenance costs of battery replacement due to the affectation of the heat for the battery duration [21].

The methodology followed in this paper is generic and can be standardized for any IoT-WHRS architecture.

Data Availability Statement: The data presented in this study are available on request from the corresponding author.

Conflicts of Interest: Authors Raúl Aragonés and Roger Malet were employed by the company Alternative Energy Innovations, S.L.—AEInnova. The remaining authors declare that the research was conducted in the absence of any commercial or financial relationships that could be construed as a potential conflict of interest.

References

1. Kweku, D.W.; Bismark, O.; Maxwell, A.; Desmond, K.A.; Danso, K.B.; Oti-Mensah, E.A.; Quachie, A.T.; Adormaa, B.B. Greenhouse effect: Greenhouse gases and their impact on global warming. *J. Sci. Res. Rep. JSRR* **2018**, *17*, 39630. [CrossRef]
2. Bianchi, G.; Panayiotou, G.P.; Aresti, L.; Kalogirou, S.A.; Florides, G.A.; Tsamos, K.; Tassou, S.A.; Christodoulides, P. Estimating the waste heat recovery in the European Union industry. *Energy Ecol. Environ.* **2019**, *4*, 211–221. [CrossRef]
3. Elahi, H.; Munir, K.; Eugeni, M.; Atek, S.; Gaudenzi, P. Energy harvesting towards self-powered IoT devices. *Energies* **2020**, *13*, 5528. [CrossRef]
4. Junior, O.H.A.; Maran, A.L.O.; Henao, N.C. A review of the development and applications of thermoelectric microgenerators for energy harvesting. *Renew. Sustain. Energy Rev.* **2018**, *91*, 376–393. [CrossRef]
5. Jouhara, H.; Khordehgah, N.; Almahmoud, S.; Delpech, B.; Chauhan, A.; Tassou, S.A. Waste heat recovery technologies and applications. *Therm. Sci. Eng. Prog.* **2018**, *6*, 268–289. [CrossRef]
6. Rodríguez, A.; Vián, J.G.; Astrain, D.; Martínez, A. Study of thermoelectric systems applied to electric power generation. *Energy Convers. Manag.* **2009**, *50*, 1236–1243. [CrossRef]
7. Patidar, S. Applications of thermoelectric energy: A review. *Int. J. Res. Appl. Sci. Eng. Technol. (IJRASET)* **2018**, *6*, 1992–1996. [CrossRef]
8. Agathokleous, R.; Bianchi, G.; Panayiotou, G.; Aresti, L.; Argyrou, M.C.; Georgiou, G.S.; Tassou, S.A.; Jouhara, H.; Kalogirou, S.A.; Florides, G.A.; et al. Waste heat recovery in the EU industry and proposed new technologies. *Energy Procedia* **2019**, *161*, 489–496. [CrossRef]
9. Biswas, K. Advances in Thermoelectric Materials and Devices for Energy Harnessing and Utilization. *J. Indian Natl. Sci. Acad.* **2015**, *81*, 903–913. [CrossRef]
10. Gayner, C.; Kar, K.K. Recent advances in thermoelectric materials. *Prog. Mater. Sci.* **2016**, *83*, 330–382. [CrossRef]
11. Radouane, N. Thermoelectric generators and their applications: Progress, challenges, and future prospects. *Chin. Phys. B* **2023**, *32*, 057307. [CrossRef]
12. Sanin-Villa, D. Recent Developments in Thermoelectric Generation: A Review. *Sustainability* **2022**, *14*, 16821. [CrossRef]
13. Pourkiaei, S.M.; Ahmadi, M.H.; Sadeghzadeh, M.; Moosavi, S.; Pourfayaz, F.; Chen, L.; Yazdi, M.A.P.; Kumar, R. Thermoelectric cooler and thermoelectric generator devices: A review of present and potential applications, modeling and materials. *Energy* **2019**, *186*, 115849. [CrossRef]
14. Sztekler, K.; Wojciechowski, K.; Komorowski, M. The thermoelectric generators use for waste heat utilization from conventional power plant. *E3S Web Conf.* **2017**, *14*, 01032. [CrossRef]
15. Oliver, J.; Malet, R.; Aragonés, R.; Voces, R.; Ferrer, C. Waste heat recovery unit for energy intensive industries Thermoelectricity Harvesting. In Proceedings of the IEEE 29th International Symposium on Industrial Electronics (ISIE), Delft, The Netherlands, 17–19 June 2020; pp. 1041–1046.
16. Sok, R.; Kusaka, J. Development and validation of thermal performances in a novel thermoelectric generator model for automotive waste heat recovery systems. *Int. J. Heat Mass Transf.* **2023**, *202*, 123718. [CrossRef]
17. Doraghi, Q.; Gora, A.Z.; Voto, G.; Krause, B.; Pötschke, P.; Ezpeleta, I.; Mateo-Mateo, C.; Jouhara, H. Experimental and computational thermoelectric generator for waste heat recovery for aeronautic application. *Energy* **2024**, *297*, 131286. [CrossRef]
18. Sanislav, T.; Mois, G.D.; Zeadally, S.; Folea, S.C. Energy harvesting techniques for internet of things (IoT). *IEEE Access* **2021**, *9*, 39530–39549. [CrossRef]
19. Zeadally, S.; Shaikh, F.K.; Talpur, A.; Sheng, Q.Z. Design architectures for energy harvesting in the Internet of Things. *Renew. Sustain. Energy Rev.* **2020**, *128*, 109901. [CrossRef]

20. Markiewicz, M.; Dziurdzia, P.; Skotnicki, T. Randomly moving thermoelectric energy harvester for wearables and industrial Internet of Things. *Nano Energy* **2024**, *126*, 109565. [CrossRef]
21. EMERSON. Power Module Life Estimator. Available online: https://tools.measurementinstrumentation.com/pervasive-sensing/power-module-life-estimator/products/12/instrument-type/21/result/ (accessed on 16 April 2024).
22. Elarusi, A.H.; Fagehi, H.; Lee, H.; Attar, A. Theoretical Approach to predict the performance of thermoelectric generator modules. *J. Electron. Mater.* **2017**, *46*, 872–881. [CrossRef]
23. Aranguren, P.; Araiz, M.; Astrain, D.; Martinez, A. Thermoelectric generators for waste heat harvesting: A computational and experimental approach. *Energy Convers. Manag.* **2017**, *148*, 680–691. [CrossRef]
24. Weera, S.L.L. Analytical Performance Evaluation of Thermoelectric Modules Using Effective Material Properties. Master's Thesis, Western Michigan University, Kalamazoo, MI, USA, 2014.
25. Alaoui, C. Peltier thermoelectric modules modeling and evaluation. *Int. J. Eng. (IJE)* **2011**, *5*, 114–121.
26. Yovanovich, M.M.; Culham, J.R.; Teertstra, P. Calculating interface resistance. *Electron. Cool.* **1997**, *3*, 24–29.
27. Lee, H. *Thermal Design: Heat Sinks, Thermoelectrics, Heat Pipes, Compact Heat Exchangers, and Solar Cells*; John Wiley & Sons, Inc.: Hoboken, NJ, USA, 2011.
28. Feng, W.; Qi, B.; Wang, Y.; Liu, H. High power DC-DC converter for renewable energy power system. In Proceedings of the IEEE Transportation Electrification Conference and Expo (ITEC Asia-Pacific), Beijing, China, 31 August–September 2014; pp. 1–4.
29. Aragonés, R.; Malet, R.; Ferrer, C.; Oliver, J. A Thermoelectric Power Generator System. U.S. Patent 20180138701A1, 24 March 2020.
30. Nab, S. Developement and Application of a computational model for thermoelectric generation out of waste heat. In *Internship Report*; Technische Universiteit Eindhoven: Eindhoven, The Netherlands, 2017.
31. Luo, D.; Wang, R.; Yu, W. Comparison and parametric study of two theoretical approaches based on an air-to-water thermoelectric generator system. *J. Power Sources* **2019**, *439*, 226079. [CrossRef]
32. Martínez, A.; Astrain, D.; Rodríguez, A. Dynamic model for simulation of thermoelectric self-cooling applications. *Energy* **2013**, *55*, 1114–1126. [CrossRef]
33. DIN ISO 10816; Why ISO 10816 Is Important for Vibration Measurement Engineers. Available online: https://www.vibsens.com/index.php/en/knowledge-base/iso10816-iso7919-charts/iso10816-charts (accessed on 16 April 2024).
34. European Commission. Ensuring That Batteries Placed on the EU Market Are Sustainable and Circular throughout Their Whole Life Cycle. Available online: https://environment.ec.europa.eu/topics/waste-and-recycling/batteries_en (accessed on 16 April 2024).